A Full Soft-Switching High Step-Up DC/DC Converter With Active Switched Inductor and Three-Winding Coupled Inductor

Chao Li, *Graduate Student Member, IEEE*, Hongzhu Li, *Member, IEEE*, Ning Wang, Xuanjin Sun, *Student Member, IEEE*, and Lihong Cheng

***Abstract*—This article proposes a full soft-switching high step-up dc/dc converter with active switched inductor and three-winding coupled inductor (ASL-TWCI). By utilizing the three-winding coupled inductor (TWCI) with a modified switched capacitor cell, the voltage gain of the ASL-TWCI is further extended without requiring an extreme duty or a high turns ratio of TWCI. Therefore, the voltage stress across the power switches is restricted. By utilizing the leakage energy of TWCI, all semiconductors achieve the zero current switching performance, which has significantly reduced the switching losses of the ASL-TWCI. Additionally, the soft-switching performance is realized by utilizing few components, which reduces the losses and improves the overall efficiency. Moreover, the construction of capacitor-clamped cell has been adjusted to decrease capacitance and voltage rating, which significantly improve the power density of ASL-TWCI. The operating principles, steady-state analysis, design, and extensive performance comparison of ASL-TWCI are described in detail. Finally, a 400 W prototype with 400 V output voltage is fabricated to verify the theoretical analysis.**

***Index Terms*—Active-switched-inductor, capacitor-clamped cell, high step-up, low voltage stress, three-winding coupled inductor.**

I. Introduction

THE technology related to dc microgrids for renewable energy sources is continuously advancing to keep up with the growing demand for energy and address concerns around the growing consumption of fossil fuel-based sources. The proportion of renewable energy sources, such as fuel cells, photovoltaic (PV) cells, and wind turbines, connected to the grid is constantly increasing. Normally, the output voltage level of renewable energy resources, such as PV, wind, and fuel cells, is low (12~48 V), which cannot directly connect to the high voltage dc bus (200~400 V). In actual converters, the influence of parasitic resistance and capacitance in inductors, equivalent series resistance (ESR) of capacitors, and other parasitic parameters prevent the classic converters from operating at ultimate duty cycle. Therefore, a high voltage conversion ratio of high-efficiency step-up dc/dc converter is urgently needed in this background.

In recent years, a series of solutions were proposed to increase the voltage conversion ratio of dc/dc converters. These approaches comprise cascade, switched inductor, switched capacitor (SC), interleaved parallel, isolated voltage doubling, magnetically coupled voltage doubling cell, coupled inductor (CI), and other voltage doubling techniques [1], [2], [3], [4], [5], [6], [7], [8], [9], [10], [11], [12], [13], [14], [15], [16], [17], [18], [19], [20], [21], [22], [23], [24], [25], [26]. Therein, the CI is a straightforward, high-efficiency, and convenient solution to achieve high voltage conversion ratio. Furthermore, the ability to regulate the turns ratio of CI provides a convenient means for adjusting the voltage conversion ratio.

Although, the leakage inductor of CI may result in high voltage spikes on semiconductors, thereby increasing voltage stresses on the semiconductors. Therefore, a series of expandable high step-up converters with the capacitor-clamped cell and CI were proposed in [5], which has added the passive clamped cell to achieve the energy recovery. Furthermore, the SC was introduced into the active-switched-inductor structure in [6]. Meanwhile, the inductors of the active-switched-inductor structure have been replaced by switched inductor in [7], [8], and [9], which have improved the voltage conversion ratio of these converters. In [10] and [11], the CI was applied to the active-switched-inductor while simultaneously utilizing the SC to further enhance the voltage conversion ratio.

Nevertheless, the high step-up dc/dc converter based on CI gradually fails to meet the actual requirements. Therefore, a series of single-switch high step-up converters with three-winding coupled inductor (TWCI) were proposed in [12], [13], [14], and [15]. However, these converters have high voltage or current stresses on the semiconductors, which may lead to the electromagnetic interference, voltage spikes, and low efficiency.

Manuscript received 25 February 2023; revised 6 May 2023; accepted 7 June 2023. Date of publication 20 June 2023; date of current version 1 September 2023. This work was supported in part by the National Natural Science Foundation of China under Grant 52177047, in part by the Natural Science Foundation of Liaoning Province under Grant 2019-MS-159, and in part by the Scientific Research Fund of Liaoning Provincial Education Department under Grant LJZK0326. Recommended for publication by Associate Editor A. Kuperman. *(Corresponding author: Hongzhu Li.)*

Chao Li, Hongzhu Li, Xuanjin Sun, and Lihong Cheng are with the Faculty of Electrical and Control Engineering, Liaoning Technical University, Huludao 125105, China (e-mail: chaoli_lc@163.com; lihongzhu@lntu.edu.cn; 472010028@stu.lntu.edu.cn; 2632689062@qq.com).

Ning Wang is with the School of Mechanical Electronic and Information Engineering, China University of Mining and Technology, Beijing 100083, China (e-mail: wn_5245@163.com).

Color versions of one or more figures in this article are available at https://doi.org/10.1109/TPEL.2023.3287974.

Digital Object Identifier 10.1109/TPEL.2023.3287974

As demonstrated in [16], [17], [18], and [19], the voltage and current stresses on semiconductors were decreased by utilizing the TWCI while also leading to further enhancements of the voltage conversion ratio. Furthermore, the active-switched-inductor structure along with TWCI was proposed in [20], [21], and [22], which has further increased the overall performance of the active-switched-inductor dc/dc converters.

Although, the converters presented in aforementioned article can achieve high voltage conversion ratio. However, the voltage stress across their output filter capacitors is equal to the output voltage, which is detrimental to the small-size and high power density requirements in dc/dc converters. Therefore, the optimized structure of capacitor-clamped cell, as presented in [23], [24], [25], and [26], is an effective method for reducing the voltage rating and capacitance requirements for output capacitors.

In order to achieve a high voltage conversion ratio dc/dc converter with soft-switching performance and few components, a full soft-switching high step-up active-switched-inductor dc/dc converter is proposed by integrating TWCI into active-switched-inductor dc/dc converter with modified capacitor-clamped cell. The voltage rating and capacitance requirements for capacitors are optimized by utilizing the modified capacitor-clamped cell. In addition, the regulation of current rise rate is achieved by utilizing the leakage inductor form TWCI, which enables all semiconductors to achieve zero current switching (ZCS) performance. And it provides good foundation for high frequency of the proposed converter in the future.

A full soft-switching high step-up dc/dc converter with active switched inductor and three-winding coupled inductor (ASL-TWCI) is proposed in this article with the following advantages.

1) Ultrahigh voltage conversion ratio is obtained by integrating a TWCI with the modified capacitor-clamped cell.
2) The rise rate of current on semiconductors is regulated by the leakage inductor, which allows for achieving the ZCS performance. The efficiency and power density of ASL-TWCI can be further enhanced.
3) The construction of the passive clamped cell is optimized to minimize the voltage rating and capacitance of the output capacitor, which make it possible to choose the capacitors with lower parasitic parameter.
4) The voltage stress across semiconductors is lower than the output voltage, allowing for the selection of semiconductors with lower parasitic parameters.

The rest of this article is organized as follows. The topology and operating principle of ASL-TWCI are described in Section II. The steady-state analysis of ASL-TWCI is presented in Section III. The efficiency and loss analysis are presented in Section IV. Section V presents the design procedure of ASL-TWCI. The comparison study and experimental results are presented in Section VI. Finally, the conclusion of this article is presented in Section VII.

II. Theoretical Analysis of ASL-TWCI

A. Topology of the ASL-TWCI

The topology of the proposed ASL-TWCI is depicted in Fig. 1. The ASL-TWCI consists of a TWCI, two power switches (S_1 and S_2), three capacitors (C_1, C_2, and C_3), and three diodes (D_1, D_2, and D_3).

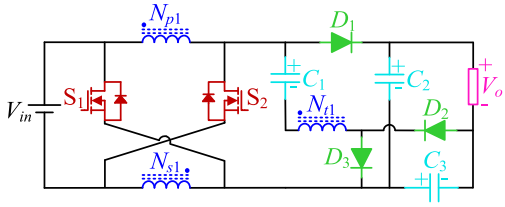

Fig. 1. Topology of the proposed ASL-TWCI.

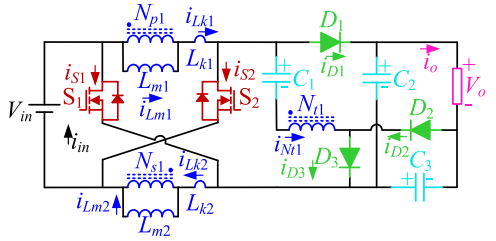

Fig. 2. Equivalent circuit of the proposed ASL-TWCI.

The two windings of TWCI are charged in parallel by the power source V_{in} when the power switches are forward biased. The two windings are discharged in series when the power switches are reverse biased. The tertiary winding and the capacitor clamped cell operate together to further increase the voltage conversion ratio of ASL-TWCI. Additionally, the conventional boost-type converters have only one filter capacitor at the output. The modified construction of the capacitor-clamped cell in ASL-TWCI can decrease the capacitance and voltage rating of capacitors, which is achieved by utilizing two filter capacitors C_2 and C_3. Therefore, it is easier to choose the capacitors with lower voltage rating and ESR, which reduces the cost and size of ASL-TWCI.

B. Operating Principle of the ASL-TWCI in Continuous Conduction Mode (CCM)

The equivalent circuit of ASL-TWCI is shown in Fig. 2. The TWCI consists of magnetizing inductor L_m, leakage inductor L_k, and the primary, secondary, and tertiary sides with turns ratio of n_{p1}, n_{s1}, and n_{t1}, respectively. Some assumptions are needed in order to analyze the circuit simply.

1) All switching components are ideal components.
2) The parasitic parameters of inductive and capacitive components are ignored.
3) The capacitors are large enough and the voltage ripple is ignored.
4) The turns ratio among N_{p1}, N_{s1}, and N_{t1} of TWCI is 1:1:n.
5) The power switches S_1 and S_2 are conducting and switching OFF simultaneously with duty cycle D.

The coupling coefficient of the TWCI is chosen as k

$$k = \frac{L_{m12}}{\sqrt{L_{m1}L_{m2}}} = \frac{L_{m13}}{\sqrt{L_{m1}L_{m3}}} = \frac{L_{m23}}{\sqrt{L_{m2}L_{m3}}} \quad (1)$$

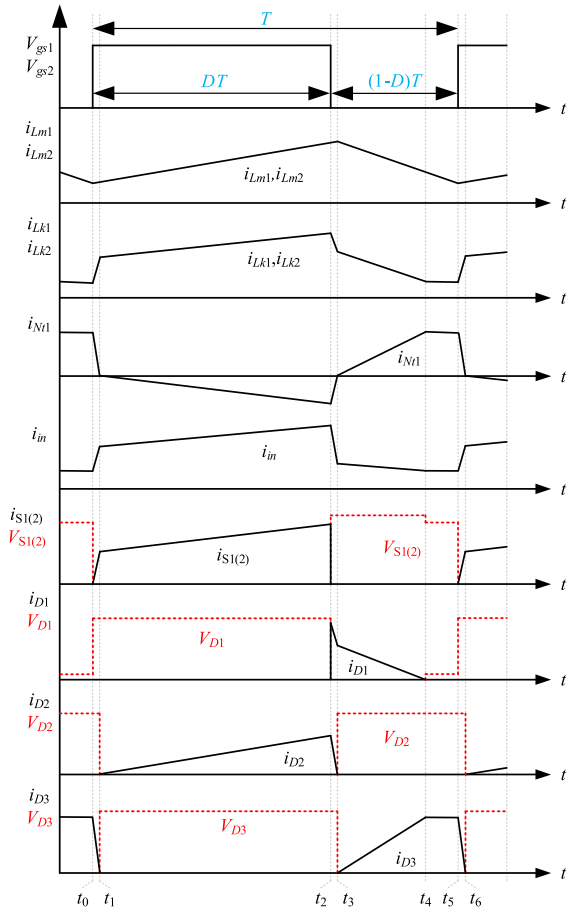

Fig. 3. Key waveform of the proposed ASL-TWCI in CCM.

where L_{m1}, L_{m2}, and L_{m3} are the independent inductances of TWCI, L_{m12} is the mutual inductance of L_{m1} and L_{m2}, L_{m13} is the mutual inductance of L_{m1} and L_{m3}, and L_{m23} is the mutual inductance of L_{m2} and L_{m3}.

Fig. 3 illustrates the key waveform in one switching cycle for CCM, which involves a total of five different modes.

Mode 1 $\{t_0 \le t \le t_1$, Fig. 4(a)$\}$: At $t = t_0$, S_1 and S_2 start to ON-state by the gating pulse signal. The D_3 is forward biased and the rest of the diodes are reverse biased. The rise rate of current on semiconductors is regulated by the leakage inductor, which enables power switches to achieve ZCS performance. The magnetizing inductors L_{m1} and L_{m2} and leakage inductors L_{k1} and L_{k2} are charged by power source V_{in}. The currents i_{Lm1}, i_{Lk1} and i_{Lm2}, i_{Lk2} increase linearly and rapidly. The load is supplied by the capacitors C_2 and C_3, and the current i_{D3} drops to zero naturally, which realizes low reverse recovery. The mode is terminated when the current i_{D3} drops to zero. According to Fig. 4(a), the following relationships are expressed as follows:

$$\begin{cases} V_{Lm1}^{\mathrm{I}} = V_{Lm2}^{\mathrm{I}} = kV_{in} \\ i_{D3}(t) = i_{D3}(t_0) - \dfrac{V_{C1} + (1+kn)V_{in}}{0.5n^2 L_k}(t - t_0). \end{cases} \tag{2}$$

Mode 2 $\{t_1 \le t \le t_2$, Fig. 4(b)$\}$: In this mode, S_1 and S_2 remain in ON-state and D_2 is forward biased. The magnetizing inductors L_{m1} and L_{m2} and leakage inductors L_{k1} and L_{k2} are charged by power source V_{in}. During this mode, the power switches remain in ON-state, which results the slower growth rate of the currents i_{Lk1} and i_{Lk2}. The mode is terminated when the power switches are in OFF-state. According to Fig. 4(b), the following relationships are expressed as follows:

$$\begin{cases} V_{Lm1}^{\mathrm{II}} = V_{Lm2}^{\mathrm{II}} = kV_{in} \\ V_{in} = V_{C3} - V_{C1} - nV_{Lm1}^{\mathrm{II}} \\ V_o = V_{C2} + V_{C3} \\ i_{D3}(t) = i_{D3}(t_1) + \dfrac{V_{C3} - V_{C1} - (1+kn)V_{in}}{0.5n^2 L_k}(t - t_1). \end{cases} \tag{3}$$

Mode 3 $\{t_2 \le t \le t_3$, Fig. 4(c)$\}$: At $t = t_2$, the S_1 and S_2 start to OFF-state. The D_1 and D_2 are forward biased and D_3 is reverse biased. The power source V_{in}, magnetizing inductors L_{m1} and L_{m2}, and leakage inductors L_{k1} and L_{k2} discharge to the load. The currents i_{Lm1}, i_{Lm2}, i_{Lk1}, and i_{Lk2} fall linearly and rapidly. This mode is a short-time transition mode, and the current i_{D2} drops to zero naturally, which realizes the low reverse recovery. The mode is terminated when the current i_{D2} drops to zero. According to Fig. 4(c), the following relationships are expressed as follows:

$$\begin{cases} V_{Lm1}^{\mathrm{III}} = V_{Lm2}^{\mathrm{III}} = \dfrac{kDV_{in}}{1-D} \\ V_{in} = V_{C3} - V_{C1} - nV_{Lm1}^{\mathrm{II}} \\ V_o = V_{C2} + V_{C3} \\ i_{D3}(t) = i_{D3}(t_2) + \dfrac{V_{C3} - V_{C1} - (1+n)V_{Lm1}^{\mathrm{III}}}{0.5n^2 L_k}(t - t_2). \end{cases} \tag{4}$$

Mode 4 $\{t_3 \le t \le t_4$, Fig. 4(d)$\}$: During this mode, the S_1 and S_2 remain in OFF-state, the D_1 and D_3 are forward biased. The load is charged by power source V_{in}, magnetizing inductors L_{m1} and L_{m2}, leakage inductors L_{k1} and L_{k2}, and capacitor C_3. The current i_{D1} drops to zero naturally, which realizes low reverse recovery. The mode is terminated when the current i_{D1} drops to zero. According to Fig. 4(d), the following relationships are expressed as follows:

$$\begin{cases} V_{Lm1}^{\mathrm{IV}} = V_{Lm2}^{\mathrm{IV}} = \dfrac{kDV_{in}}{1-D} \\ V_{Lk1}^{\mathrm{IV}} = V_{Lk2}^{\mathrm{IV}} \\ V_{in} = 2\left(V_{Lm1}^{\mathrm{IV}} + V_{Lk1}^{\mathrm{IV}}\right) + V_{C2} \\ V_{C2} = V_{C1} + nV_{Lm1}^{\mathrm{IV}} \\ i_{D3}(t) = i_{D3}(t_3) - \dfrac{V_{in} + V_{C1} + nV_{Lm1}^{\mathrm{IV}}}{0.5n^2 L_k}(t - t_3). \end{cases} \tag{5}$$

Mode 5 $\{t_4 \le t \le t_5$, Fig. 4(e)$\}$: During this mode, the S_1 and S_2 remian in OFF-state and D_3 is forward biased. The C_1 is charged by power source V_{in}, magnetizing inductors L_{m1} and L_{m2}, leakage inductors L_{k1} and L_{k2}, and tertiary winding N_{t1}. The load is supplied by the capacitors C_2 and C_3. The mode is terminated when the power switches are in the ON-state. According to Fig. 4(e), the following relationships are expressed

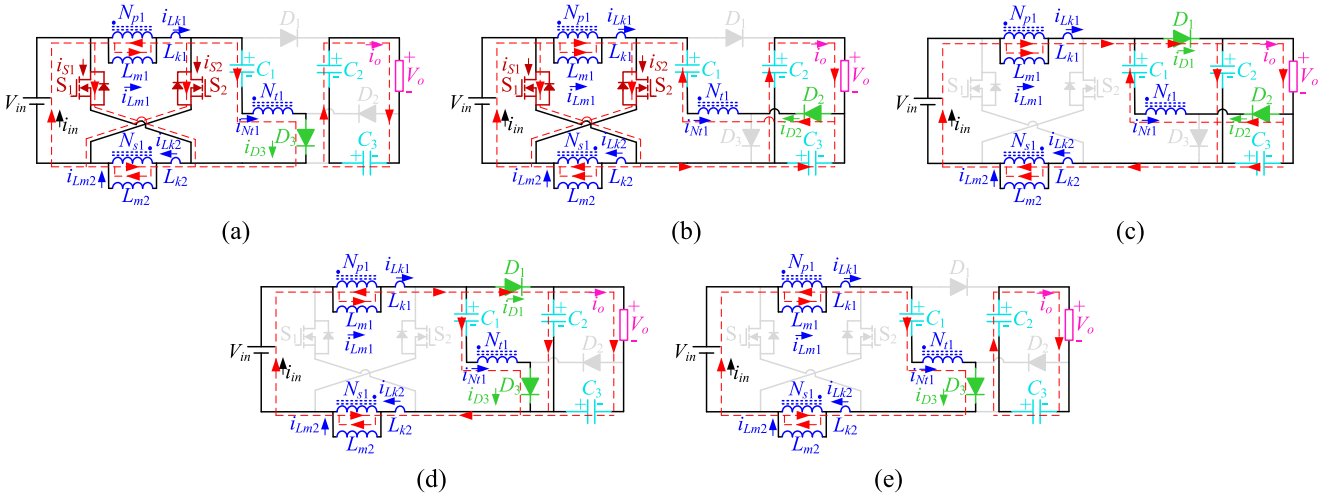

Fig. 4. Operation modes of ASL-TWCI in CCM. (a) Mode 1 [$t_0 \sim t_1$]. (b) Mode 2 [$t_1 \sim t_2$]. (c) Mode 3 [$t_2 \sim t_3$]. (d) Mode 4 [$t_3 \sim t_4$]. (e) Mode 5 [$t_4 \sim t_5$].

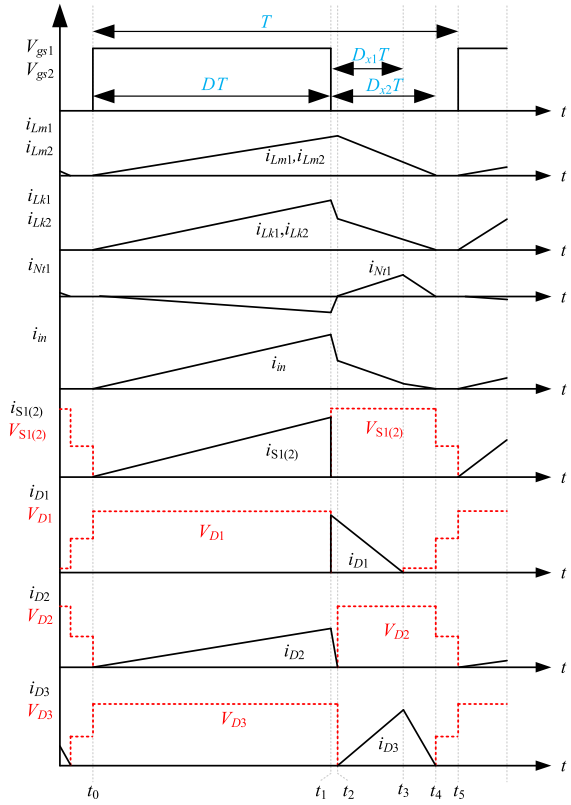

Fig. 5. Key waveform of the proposed ASL-TWCI in DCM.

as follows:

$$\begin{cases} V_{Lm1}^{\mathrm{V}} = V_{Lm2}^{\mathrm{V}} \\ V_{Lk1}^{\mathrm{V}} = V_{Lk2}^{\mathrm{V}} \\ V_o = V_{C2} + V_{C3} \\ i_{D3}(t) = i_{D3}(t_4) - \dfrac{V_{in} + V_{C1} + nV_{Lm1}^{\mathrm{V}}}{0.5n^2 L_k}(t - t_4). \end{cases} \tag{6}$$

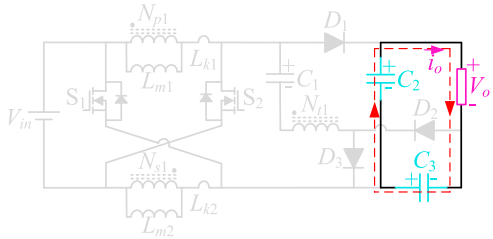

Fig. 6. Equivalent circuits for mode 5 of ASL-TWCI in DCM.

C. Operating Principle of the ASL-TWCI in DCM

Fig. 5 illustrates the key waveforms of ASL-TWCI in discontinuous conduction mode (DCM). The modes 1, 2, 3, and 4 in DCM are similar to modes 2, 3, 4, and 5 in CCM. Therefore, the mode 5 in DCM is discussed in Fig. 6.

Mode 5 $\{t_4 \le t \le t_5$, Fig. 6$)\}$: During this mode, all semiconductors are reverse biased. The load is supplied by the capacitors C_2 and C_3.

III. Steady-State Analysis of ASL-TWCI

A. Voltage Gain of the ASL-TWCI

For the simplification of the steady-state analysis, the two transitional modes 1 and 3 are neglected. By employing the KVL and the voltage-second balance principle, the voltage rating of capacitors can be obtained by solving (1)–(6)

$$\begin{cases} V_{C1} = \dfrac{k(n+2)D + 1 - D}{1 - D} V_{in} \\ V_{C2} = \dfrac{2kD + 1 - D}{1 - D} V_{in} \\ V_{C3} = \dfrac{k(n+2)}{1 - D} V_{in} \end{cases} \tag{7}$$

where k is the coupling coefficient, n is the turns ratio of TWCI, V_{in} is the input voltage, and D is the duty cycle.

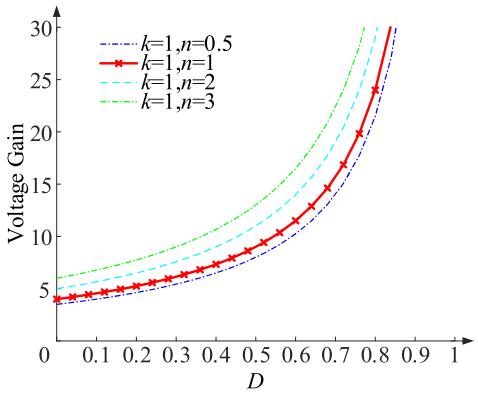

Fig. 7. Relationship among n, D, and voltage gain.

Based on (3)–(7), the voltage gain of ASL-WTCI can be calculated as follows:

$$G = \frac{V_o}{V_{in}} = \frac{k(n+2+2D)+1-D}{1-D}. \tag{8}$$

According to (8), the voltage gain of ASL-TWCI is related to the coupling coefficient k, turns ratio n, and duty cycle D. The curve of the voltage gain for different values of n and D is illustrated in Fig. 7.

According to Fig. 7, the voltage gain of ASL-TWCI is proportional to the turns ratio n, and duty cycle D. There is a greater impact on the voltage gain by the turns ratio n and duty cycle D. The coupling coefficient k has a negligible effect on voltage gain when compared with the turns ratio n and duty ratio D.

When the coupling coefficient is $k = 1$, (8) can be rewritten as follows:

$$G = \frac{V_o}{V_{in}} = \frac{3+n+D}{1-D}. \tag{9}$$

B. Voltage and Current Stress of ASL-TWCI

According to (7) and (8), the voltage stress across the capacitors C_1, C_2, and C_3 can be rewritten as follows:

$$\begin{cases} V_{VpsC1} = \dfrac{k(n+2)D+1-D}{k(n+2+2D)+1-D}V_o \\ V_{VpsC2} = \dfrac{2kD+1-D}{k(n+2+2D)+1-D}V_o \\ V_{VpsC3} = \dfrac{k(n+2)}{k(n+2+2D)+1-D}V_o. \end{cases} \tag{10}$$

According to (10), the voltage stress across the capacitors is mainly influenced by the duty cycle D and turns ratio n. Additionally, the voltage stress of C_1, C_2, and C_3 is much lower than the output voltage.

According to (7) and the equivalent circuits of ASL-TWCI, the voltage stress across semiconductors can be calculated as follows:

$$\begin{cases} V_{VpsS1} = V_{VpsS2} = \dfrac{1}{k(n+2+2D)+1-D}V_o \\ V_{VpsD1} = \dfrac{2(kD+1-D)}{k(n+2+2D)+1-D}V_o \\ V_{VpsD2} = V_{VpsD3} = \dfrac{k(n+2)}{k(n+2+2D)+1-D}V_o. \end{cases} \tag{11}$$

As seen from (11), the voltage stress across power switches and diodes is significantly lower than the output voltage. Therefore, it is possible to choose the power switches with lower voltage rating and internal resistances, as well as diodes with lower voltage and internal resistance, which significantly increases the efficiency of ASL-TWCI.

C. Influence of Leakage Inductor

According to the operation principle of ASL-TWCI, the leakage inductor has a great influence on voltage gain. Due to the nonlinear relationship among leakage inductor, voltage gain, and voltage stress, it is not possible to be simply expressed by the coupling coefficient k. In this section, the effect of leakage inductor on voltage gain of ASL-TWCI is described in detail.

When the power switches remain in ON-state, the voltage of leakage inductor can be written as follows:

$$V_{Lk\_\text{on}} = L_k \frac{nI_o f_s}{D^2} \tag{12}$$

where L_k is the leakage inductor of TWCI, n is the turns ratio of TWCI, I_o is the output current, f_s is the switching frequency, and D is the duty cycle.

When the power switches remain in OFF-state, the voltage of leakage inductor can be written as follows:

$$V_{Lk\_\text{off}} = L_k \frac{nI_o f_s}{(1-D)^2}. \tag{13}$$

By considering the leakage inductor of TWCI, (3) can be rewritten as follows:

$$\begin{cases} V_{Lm1}^{\text{II}} = V_{Lm2}^{\text{II}} = V_{in} - V_{Lk\_\text{on}} \\ V_{in} = V_{C3} - V_{C1} - n(V_{in} - V_{Lk\_\text{on}}) \\ V_o = V_{C2} + V_{C3}. \end{cases} \tag{14}$$

By considering the leakage inductor of TWCI, (4) can be rewritten as follows:

$$\begin{cases} V_{Lm1}^{\text{IV}} = V_{Lm2}^{\text{IV}} = V_{in} - V_{Lk\_\text{off}} \\ V_{in} = 2\left(V_{in} + V_{Lm1}^{\text{IV}} - V_{Lk\_\text{off}}\right) + V_{C2} \\ V_{C2} = V_{C1} + V_{in} - V_{Lk\_\text{off}}. \end{cases} \tag{15}$$

By solving (12)–(15) and the voltage-second balance, the voltage rating of capacitors can be calculated as follows:

$$\begin{cases} V_{C1} = \dfrac{(1+nD+D)D^2V_{in} - I_oL_kf_sn(2+nD)}{(1-D)D^2} \\ V_{C2} = \dfrac{(1+D)D^2V_{in} - 2I_oL_kf_sn}{(1-D)D^2} \\ V_{C3} = \\ \dfrac{(n+2)^2D^3V_{in} - I_oL_kf_sn(D(2nD+n^2+4)+2n)}{(1-D)D^3(n+2)}. \end{cases} \tag{16}$$

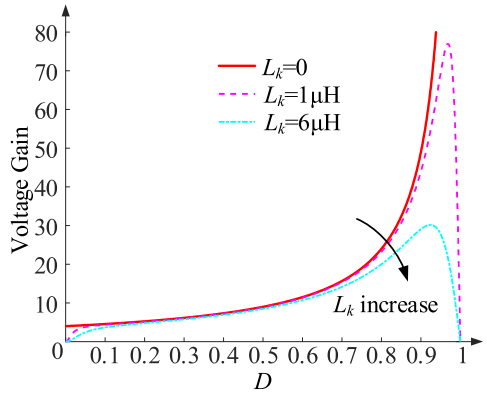

Fig. 8. Voltage gain considering the effect of the leakage inductor.

According to (14) and (16), the voltage gain from the influence of leakage inductor is written as follows:

$$G = \frac{V_o}{V_{in}} = \frac{(n - nD + 3 - 2D - D^2)D^2}{(1-D)^2D^2 - \frac{L_k f_s n}{R}(nD - n - 4D)} \tag{17}$$

where n is the turns ratio of TWCI, D is the duty cycle, L_k is the leakage inductor of TWCI, f_s is the switching frequency, and R is the resistance of load.

According to (17), the voltage gain of ASL-TWCI is related to the leakage inductor L_k, turns ratio n, load R, and duty cycle D. The switching frequency and the load of actual circuit are generally considered as fixed values. By varying the duty cycle D, turn ratio n, and leakage inductor L_k, the voltage gain of ASL-TWCI can be changed. The relationship between the leakage inductor and voltage gain is shown in Fig. 8 when the turns ratio is chosen as $n = 1$ and the switching frequency of ASL-TWCI is 100 kHz.

As seen from Fig. 8, the actual voltage conversion ratio significantly deviates from the theoretical voltage gain when the ASL-TWCI is operating at extreme duty cycle. Therefore, it is not appropriate to make the ASL-TWCI work in extreme duty cycle.

D. Boundary Conduction Mode (BCM)

According to Fig. 5, the following relationships are achieved by employing the KVL and voltage-second balance principle:

$$\begin{cases} V_{C1} = \dfrac{(kn+2)D + D_{x2}}{D_{x2}} V_{in} \\ V_{C2} = \dfrac{2D + D_{x2}}{D_{x2}} V_{in} \\ V_{C3} = \dfrac{(kn+2)(D + D_{x2})}{D_{x2}} V_{in}. \end{cases} \tag{18}$$

From Fig. 5 and (18), the voltage gain in DCM is derived as follows:

$$G_{\text{DCM}} = \frac{V_o}{V_{in}} = \frac{(4+kn)D + (3+kn)D_{x2}}{D_{x2}} \tag{19}$$

where D is the turn-ON time of power switches, D_{x1} is the turn-ON time of diode D_1, and D_{x2} is the turn-ON time of diode D_2.

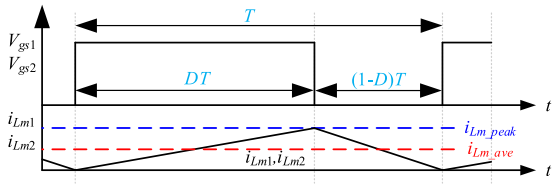

Fig. 9. Key waveform of the proposed ASL-TWCI in BCM.

The maximum current of magnetizing inductor i_{Lm_peak} can be derived as follows:

$$i_{Lm\_\text{peak}} = \frac{V_{in} DT}{L_m} \tag{20}$$

where T represents the time of one switching period, and L_m is the inductance of magnetizing inductor.

The peak and average currents of the diodes can be determined by applying the ampere-second balance principle of capacitors C_1, C_2, and C_3

$$\begin{cases} I_{D1\_\text{peak}} = i_{Lm\_\text{peak}} \\ I_{D3,\text{ave}} = \dfrac{D_{x1}}{D_{x2}} i_{Lm\_\text{peak}} \end{cases} \tag{21}$$

$$I_{D1,\text{ave}} = I_{D2,\text{ave}} = I_{D3,\text{ave}} = I_o. \tag{22}$$

According to Fig. 5 and voltage-second balance principle of magnetizing inductor, the follow relationships can be derived:

$$\begin{cases} \dfrac{1}{T}\left(\dfrac{i_{Lm\_\text{peak}} D_{x1} T}{2}\right) \\ = \dfrac{\int_{DT}^{(D+D_{x1})T} (i_{D1} + (1+0.5n) i_{D3})\, dt}{T} \\ \dfrac{1}{T}\left(\dfrac{i_{Lm\_\text{peak}} D_{x2} T}{2}\right) = \dfrac{1}{T}\displaystyle\int_{(D+D_{x1})T}^{(D+D_{x2})T} (1+0.5n) i_{D3} dt \\ + \dfrac{1}{T}\displaystyle\int_{DT}^{(D+D_{x1})T} (i_{D1} + (1+0.5n) i_{D3})\, dt. \end{cases} \tag{23}$$

From (23), D_{x1} and D_{x2} can be achieved as follows:

$$\begin{cases} D_{x1} = \dfrac{1-D}{2+n+D} \\ D_{x2} = \dfrac{2(2+0.5n) I_o L_m}{D V_{in} T}. \end{cases} \tag{24}$$

According to Fig. 9, $D_{x2} = 1 - D$ when the ASL-TWCI operates in BCM. Equation (24) can be rewritten as follows:

$$1 - D = \frac{2(2+0.5n) V_o}{D V_{in}} \frac{L_m}{RT}. \tag{25}$$

The time constant of magnetizing inductor can be defined as follows:

$$\tau_{Lm} = \frac{L_m}{RT} \tag{26}$$

where τ_{Lm} is the time constant of magnetizing inductor. According to (9) and (20)–(26), the time constant τ_{Lm} in BCM is calculated as follows:

$$\tau_{Lm} = \frac{D(1-D)^2}{2(2+0.5n)(3+n+D)}. \tag{27}$$

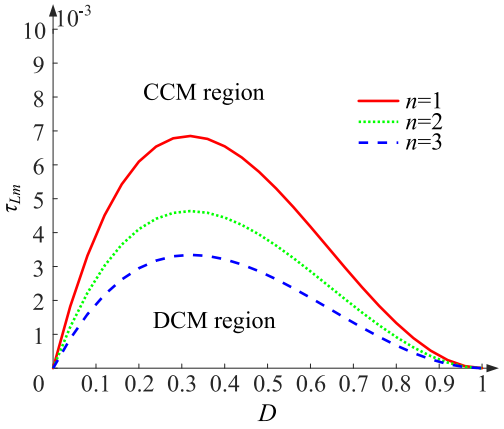

Fig. 10. Boundary condition of the proposed ASL-TWCI.

According to (27), the boundary condition of the proposed ASL-TWCI is shown in Fig. 10.

E. Analysis of ZCS Condition

According to Mode 1 in CCM, the rising rate of currents i_{S1}, i_{S2} and the falling rate of currents i_{D1}, i_{D2}, i_{D3} are affected by the leakage inductor. Therefore, the ZCS performance of power switches S_1 and S_2 is accomplished by utilizing the reasonable leakage inductor, which is also beneficial in alleviating the issue of reverse recovery in the diodes. According to (2) and (12), the leakage inductor L_k can be calculated as follows:

$$L_k = \frac{D^2(V_{C1} + (1+kn)V_{in})}{0.5n^3 I_o f_s}. \tag{28}$$

IV. Efficiency and Loss Analysis of the Proposed Converter

The losses of ASL-TWCI mainly includes the power switches, diodes, capacitors, and magnetic component.

A. Switches and Diodes' Losses

The losses of power switches include the conduction loss and switching loss. In this article, the power switches achieve ZCS performance by utilizing the leakage energy of TWCI. Therefore, the losses of power switches are calculated as follows:

$$P_S = I_{rms\_S1}^2 R_{S1} + I_{rms\_S2}^2 R_{S2} + \frac{(V_{S1}^2 + V_{S2}^2)C_r + (V_{S1} I_{S1\_off} + V_{S2} I_{S2\_off})t_f}{2} f_s \tag{29}$$

where R_{S1} and R_{S2} are the ON-resistances of power switches, I_{rms_S1} and I_{rms_S2} are the rms currents of power switches, t_f is the falling time of power switches, C_r is the output capacitor of power switches, V_{S1} and V_{S2} are the voltages at switch-OFF, and I_{S1_off} and I_{S2_off} are the current stresses at switch-OFF. And the rms currents of power switches are as follows:

$$I_{rms\_S1} = I_{rms\_S2} = \frac{I_o}{2(1-D)} \sqrt{\frac{(3n^2 + 12n + 3D + 25)D^2 + 4(3nD + D + 4)}{3D}}. \tag{30}$$

Because of the leakage inductor of TWCI, the reverse recovery loss of diodes is zero and neglected and the diodes turn OFF naturally. The losses of diodes can be calculated as follows:

$$P_D = \sum_{i=1,2,3} \left(V_{FDi} I_o + I_{rms\_Di}^2 r_{Di}\right) \tag{31}$$

where V_{FDi} is the forward voltage drop of diodes, I_o is the output current, r_{Di} is the ON-resistance, and the rms current I_{rms_Di} of diodes is expressed as follows:

$$\begin{cases} I_{rms\_D1} = I_o \sqrt{\dfrac{n+D+5}{2(1-D)} - \dfrac{6(n^2+D^2+2n(3+D)+6D)-2}{3(1-D)(n+1+D)^3}} \\ I_{rms\_D2} = \dfrac{2I_o}{\sqrt{3D}} \\ I_{rms\_D3} = \dfrac{2I_o}{\sqrt{3(1-D)}}. \end{cases} \tag{32}$$

B. TWCI and Capacitors' Losses

The losses of TWCI mainly include the magnetic loss and copper loss

$$P_{CI} = P_{cu,CI} + P_{core,CI}. \tag{33}$$

The loss of the magnetic core can be expressed as follows:

$$P_{core,CI} = K_c f_s^{\delta} B_{max}^{\beta} A_c l_c \tag{34}$$

where B_{max} is the maximum flux of magnetic component under the excitation of f_s, A_c is the window area of magnetic component, l_c is the equivalent core length, and K_c, δ, and β are the empirical constants.

The copper loss can be expressed as follows:

$$P_{cu,CI} = I_{rms\_Lk1}^2 r_{Lk1} + I_{rms\_Lk2}^2 r_{Lk2} + I_{rms\_Nt1}^2 r_{Nt1} \tag{35}$$

where I_{rms_Lk1}, I_{rms_Lk2}, and I_{rms_Nt1} are the rms currents of TWCI, and r_{Lk1}, r_{Lk2}, and r_{Nt1} are the resistances of TWCI

$$\begin{cases} I_{rms\_Lk1} = I_{rms\_Lk2} = \dfrac{I_o}{2(1-D)} \sqrt{\dfrac{(3n^2 + 6n(5-D) + (10-9D)D + 31)D + 16}{3D}} \\ I_{rms\_Nt1} = \dfrac{2I_o}{\sqrt{3D(1-D)}}. \end{cases} \tag{36}$$

The loss of capacitors can be expressed as follows:

$$P_c = \sum_{i=1,2,3} I_{rms\_ci}^2 R_{ci} \tag{37}$$

TABLE I
PARAMETERS OF THE ASL-TWCI

Parameter/Component	Specification
Input voltage V_{in}	36 V
Output voltage V_o	400 V
Rated power P_o	400 W
Turns ratio	N_p:N_s:N_t = 1:1:1
Magnetizing inductance L_{m1}	90.952 μH
Magnetizing inductance L_{m2}	90.417 μH
Leakage inductance L_{k1}	1.793 μH
Leakage inductance L_{k2}	1.617 μH
Capacitance C_1	4.7 μF/250 V
Capacitance C_2	4.7 μF /250 V
Capacitance C_3	10 μF /450 V
Diode D_1	MBR10200CT
Diodes D_2 & D_3	ASD265D
Power switches	IPB108N15N3 G
Switching frequency f_s	100 kHz

where R_{ci} is the parasitic resistance of capacitors, and the rms currents of capacitors are calculated as follows:

$$\begin{cases} I_{\text{rms\_}C1} = \dfrac{2I_o}{\sqrt{3D(1-D)}} \\ I_{\text{rms\_}C2} = I_o \sqrt{\dfrac{6(n^2(2D-3)+2n(2D^2-3D-3) \\ +2D^3-3D^2-8D)+14}{3(1-D)(1+n+D)^3} + \dfrac{n+3+3D}{2(1-D)}} \\ I_{\text{rms\_}C3} = I_o\sqrt{\dfrac{4-3D}{3D}}. \end{cases} \tag{38}$$

The overall loss of ASL-TWCI is calculated as follows:

$$P_{\text{Loss}} = P_{\text{S}} + P_D + P_c + P_{\text{CI}}. \tag{39}$$

The efficiency of ASL-TWCI is calculated as follows:

$$\eta = \frac{P_o}{P_o + P_{\text{Loss}}} \tag{40}$$

where P_o represents the output power.

V. Design Procedure of ASL-TWCI

A 400 W prototype of ASL-TWCI has been built and a variety of measurements are performed to measure its performance. The prototype operates in CCM and the parameters of experimental prototype are stated in Table I. And the design steps of ASL-TWCI is shown in Fig. 11.

A. Design of TWCI

According to (9), the turns ratio of TWCI and duty cycle D are related to the voltage gain. Therefore, the turns ratio of TWCI is calculated as follows:

$$n \geq (1-D)\frac{V_o}{V_{in}} - 3 - D. \tag{41}$$

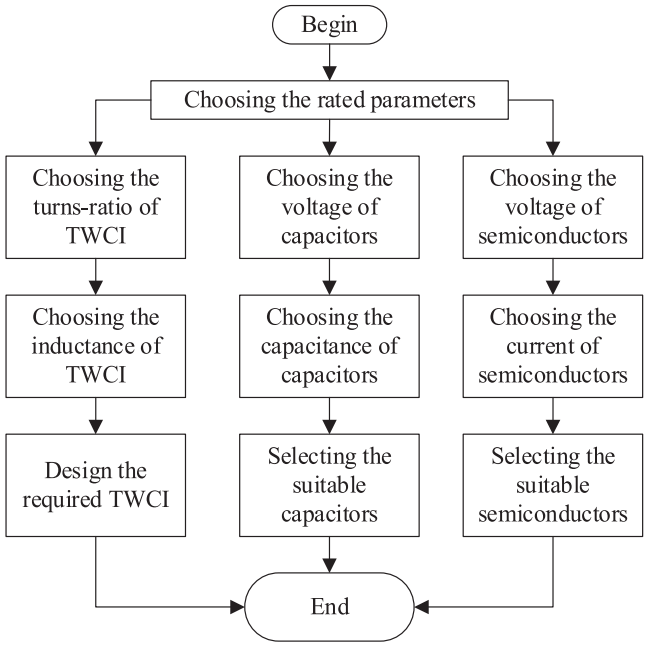

Fig. 11. Design steps of ASL-TWCI.

The duty cycle D is taken as 0.6, so the turns ratio is taken as $n = 1$.

By considering the maximum ripple current and selecting the ripple current coefficient as γ, the maximum current ripple can be calculated as follows:

$$I_{Lm1} = I_{Lm2} = \frac{\Delta i_{Lm1\max}}{\gamma} = \frac{\Delta i_{Lm2\max}}{\gamma}. \tag{42}$$

The inductance of TWCI can be calculated as follows:

$$L_{m1}{=}L_{m2} \geq \frac{V_{in}D}{\Delta i_{Lm1\max} f_s} = \frac{V_{\text{in}}D}{\gamma I_{Lm1} f_s}. \tag{43}$$

When the current ripple coefficient is chosen as $\gamma = 0.4$, According to (42) and (43), the inductance of TWCI should be greater than 75 μH. Therefore, the inductance of TWCI is taken as 90 μH.

B. Design of Capacitors

The voltage rating of capacitors has been calculated in (10). The capacitance of capacitors is determined by the power and maximum ripple coefficient of output voltage. The ripple coefficient is assumed as α. And the capacitance of capacitors can be calculated as follows:

$$\begin{cases} C_{C1} \geq \dfrac{I_o}{\Delta V_{C1} f_s} = \dfrac{k(n+2+2D)+1-D}{(kD(n+2)+1-D)\alpha V_o^2 f_s} P_o \\ C_{C2} \geq \dfrac{I_o}{\Delta V_{C2} f_s} = \dfrac{k(n+2+2D)+1-D}{(2kD+1-D)\alpha V_o^2 f_s} P_o \\ C_{C3} \geq \dfrac{I_o}{\Delta V_{C3} f_s} = \dfrac{k(n+2+2D)+1-D}{k(n+2)\alpha V_o^2 f_s} P_o. \end{cases} \tag{44}$$

The ripple coefficient of output voltage is taken as $\alpha = 0.03$. According to (44), the capacitance of C_{C1} is calculated as 1.724 μF, the capacitance of C_{C2} is calculated as 2.396 μF, and the capacitance of C_{C3} is calculated as 1.248 μF. Considering the actual capacitor value, the capacitance of C_{C1}andC_{C2} is selected as 4.7 μF and C_{C3} is selected as 10 μF.

According to the design of components, the major components of ASL-TWCI are shown in Table I.

The value of the components' parameters is considered as: $r_{\mathrm{S1}} = r_{\mathrm{S}_2} = 10.8\ \ \mathrm{m\Omega}$, $t_{\mathrm{off}} = 9\ \ \mathrm{ns}$, and $C_{oss} = 378\ \ \mathrm{pF}$; $r_{D1} = 5\ \ \mathrm{m\Omega}$ and $V_{FD1} = 0.68\,\mathrm{V}$; $r_{D2} = r_{D3} = 10\ \ \mathrm{m\Omega}$ and $V_{FD2} = 1.38\,\mathrm{V}$; $r_{C1} = r_{C2} = 5.39\ \ \mathrm{m\Omega}$, $r_{C3} = 6.56\ \ \mathrm{m\Omega}$, $r_{Np1} = r_{Ns1} = 19\ \ \mathrm{m\Omega}$, and $r_{Nt1} = 23\ \ \mathrm{m\Omega}$.

C. Small-Signal Modeling of the ASL-TWCI

Assuming that the ASL-TWCI operates in CCM, the small-signal modeling can be obtained by utilizing the state-space averaging method. The state variables are the independent currents of inductors and the voltages across capacitors. As a result, we can select the state vector x as follows:

$$x = \begin{bmatrix} i_{Lm1} & i_{Lm2} & i_{Nt1} & V_{C1} & V_{C2} & V_{C2} \end{bmatrix}. \tag{45}$$

The state-space equation of ASL-TWCI can expressed as follows:

$$\begin{cases} \dfrac{\mathrm{dx}}{dt} = Ax + Bu \\ y = Cx + Du. \end{cases} \tag{46}$$

The state-space equation is expressed as (47) shown at the bottom of this page when power switches are in ON-state, while the state-space equation is expressed as (48) shown at the bottom of this page when the power switches are in OFF-state

$$\begin{cases} A = A_1 + A_2 \\ B = B_1 + B_2 \\ C = C_1 + C_2 \\ D = D_1 + D_2. \end{cases} \tag{49}$$

To obtain the small-signal model, it is necessary to decompose the average variables into dc components and ac small-signal components

$$\begin{cases} d = D + \widehat{d} \\ x = X + \widehat{x} \\ u = U + \widehat{u}. \end{cases} \tag{50}$$

According to (45)–(50), the control to output transfer function can be expressed as follows:

$$\begin{aligned} G_{yd}(s) &= \left.\frac{\widehat{y}(s)}{\widehat{d}(s)}\right|_{\widehat{v}_{in}=0} \\ &= C(sI - A)^{-1}((A_1 - A_2)X + (B_1 - B_2)V_{in}) \\ &\quad + (C_1 - C_2)X + (D_1 - D_2)V_{in}. \end{aligned} \tag{51}$$

According to the parameter values in Table I, the bode plot for the control to output transfer function is shown in Fig. 12.

$$\begin{cases} \dfrac{dx}{dt} = \begin{bmatrix} 0 & 0 & 0 & 0 & 0 & 0 \\ 0 & 0 & 0 & 0 & 0 & 0 \\ 0 & 0 & 0 & -\dfrac{k}{n^2 L_m} & 0 & \dfrac{k}{n^2 L_m} \\ 0 & 0 & \dfrac{1}{C_1} & 0 & 0 & 0 \\ 0 & 0 & 0 & 0 & 0 & 0 \\ 0 & 0 & \dfrac{1}{C_3} & 0 & 0 & 0 \end{bmatrix} \begin{bmatrix} i_{Lm1} \\ i_{Lm2} \\ i_{Nt1} \\ V_{C1} \\ V_{C2} \\ V_{C3} \end{bmatrix} + \begin{bmatrix} \dfrac{k}{L_m} \\ \dfrac{k}{L_m} \\ -\dfrac{k}{n^2 L_m} \\ 0 \\ -\dfrac{n+D+3}{C_2 R(1-D)} \\ \dfrac{n+D+3}{C_3 R(1-D)} \end{bmatrix} V_{in} = A_1 x + B_1 u \\ y = \begin{bmatrix} 0 & 0 & 0 & 0 & 1 & 1 \end{bmatrix} x + [0]\, u = C_1 x + D_1 u \end{cases} \tag{47}$$

$$\begin{cases} \dfrac{dx}{dt} = \begin{bmatrix} 0 & 0 & 0 & 0 & -\dfrac{k}{2L_m} & 0 \\ 0 & 0 & 0 & 0 & -\dfrac{k}{2L_m} & 0 \\ 0 & 0 & 0 & -\dfrac{k}{n^2 L_m} & \dfrac{k}{n^2 L_m} & 0 \\ 0 & 0 & \dfrac{1}{C_1} & 0 & 0 & 0 \\ \dfrac{1}{C_2} & 0 & -\dfrac{1}{C_2} & 0 & 0 & 0 \\ 0 & 0 & 0 & 0 & 0 & 0 \end{bmatrix} \begin{bmatrix} i_{Lm1} \\ i_{Lm2} \\ i_{Nt1} \\ V_{C1} \\ V_{C2} \\ V_{C3} \end{bmatrix} + \begin{bmatrix} \dfrac{k}{2L_m} \\ \dfrac{k}{2L_m} \\ 0 \\ 0 \\ -\dfrac{n+D+3}{C_2 R(1-D)} \\ -\dfrac{n+D+3}{C_3 R(1-D)} \end{bmatrix} V_{in} = A_2 x + B_2 u \\ y = \begin{bmatrix} 0 & 0 & 0 & 0 & 1 & 1 \end{bmatrix} x + [0]\, u = C_2 x + D_2 u \end{cases} \tag{48}$$

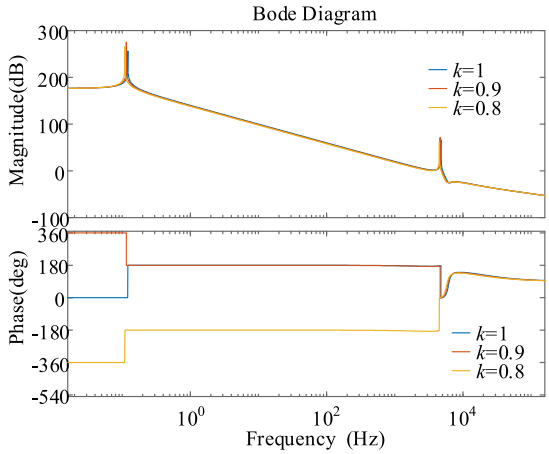

Fig. 12. Bode for control to output transfer function.

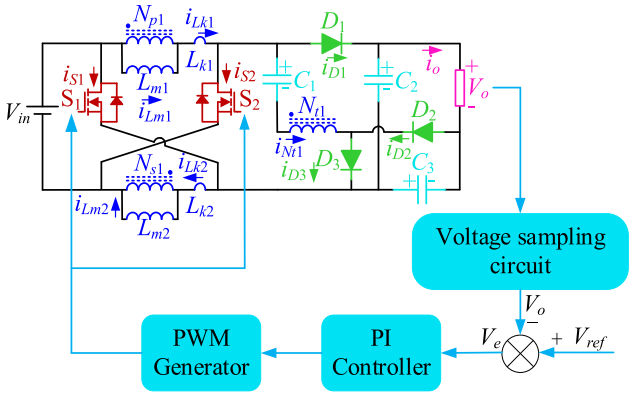

Fig. 13. Schematic control diagram of ASL-TWCI.

D. Schematic Control Diagram of ASL-TWCI

The schematic control diagram of ASL-TWCI is presented in Fig. 13. The output voltage V_o of ASL-TWCI is measured by the sampling circuit, with V_{ref} being the reference voltage. Any deviation between the reference voltage V_{ref} and output voltage V_o is represented by error value V_e. To ensure the reliability of ASL-TWCI, the PI controller modifies the duty cycle D according to the error value V_e. And the pulsewidth modulation (PWM) generator creates the PWM pulse signal for power switches.

VI. Comparative Study and Results Analysis

A. Comparative Study

This section presents a comparative study to demonstrate the advantages of ASL-TWCI and verify its benefits. Table II presents a summary of major performance for ASL-TWCI in comparison with other similar converters that use CI and TWCI. Table II summarizes the number of power switches, diodes, capacitors, voltage gain, voltage stress, soft switching, and magnetic components.

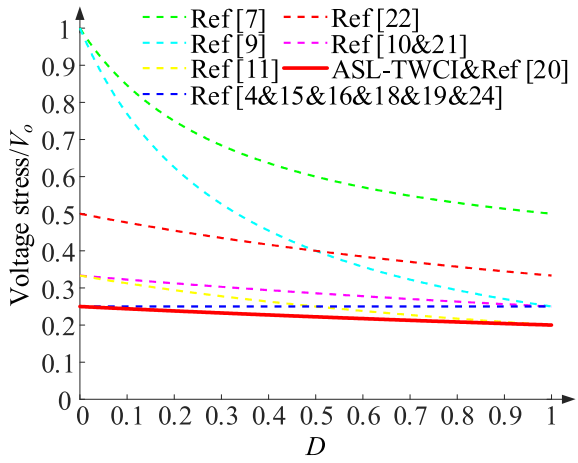

Fig. 14. Normalized voltage stress comparison between ASL-TWCI and other similar converters when $n = 1$.

The voltage gain and the number of components in ASL-TWCI are identical to the converter presented in [20]. However, it has only one filter capacitor at the output in [20]. The ASL-TWCI has two filter capacitors that can effectively reduce the voltage rating and capacitance of the filter capacitors. Therefore, the power density and efficiency of the ASL-TWCI are effectively improved.

The converters achieve lower voltage gain and higher voltage stress on the switches with more devices in [4], [7], [9], [10], [11], [15], [16], [18], [19], [21], [22], and [24]. Compared with the other converters where the switching components are hard or partially soft switching, all of the switching components in ASL-TWCI can operate under ZCS performance, which improve the overall efficiency of the ASL-TWCI. And the soft-switching characteristics of ASL-TWCI provide the foundation for high frequency.

The voltage gain versus D of all other references is less than the ASL-TWCI one and the trend is similar. In Fig. 14, a comparison was made between the voltage stress across power switches in ASL-TWCI and other similar converters, as listed in Table II. According to the previous discussions, it has been concluded that ASL-TWCI has a series of advantages over other existing converters. These benefits include high voltage conversion ratio, low voltage stress on components, fewer components required, soft switching of all semiconductors, and suitability for high-power applications. Furthermore, the ASL-TWCI has lower voltage rating and capacitance requirements for capacitors.

B. Simulation Analysis

Before building the experimental prototype, the simulation for ASL-TWCI is built to verify its performance. And the simulation parameter values are given in Table I. The simulation study for ASL-TWCI in all operating modes is conducted in CCM. The simulation waveforms of ASL-TWCI are illustrated in this section.

TABLE II
COMPARAISON OF THE PROPOSED CONVERTER WITH OTHER EXISTED CONVERTER

Converter	Voltage gain	No. switches	No. diodes	No. capacitors	No. CIs	Voltage stress of switch	Soft switching	Power	Efficiency
ASL-TWCI	$\frac{3+n+D}{1-D}$	2	3	3	1	$\frac{V_o}{3+n+D}$	ZCS	400 W	97.91%
[4]	$\frac{1+3n}{1-D}$	2	5	4	2	$\frac{V_o}{1+3n}$	ZCS	400 W	97%
[7]	$\frac{1+3D}{1-D}$	2	7	1	4	$\frac{1+D}{1+3D}V_o$	--	200 W	--
[9]	$\frac{1+(2n+1)D}{1-D}$	3	3	3	2	$\frac{V_o}{1+(2n+1)D}$	--	400 W	--
[10]	$\frac{3+D}{1-D}$	2	3	3	2	$\frac{V_o}{3+D}$	--	200 W	96.2%
[11]	$\frac{2+n+(n+1)D}{1-D}$	2	5	5	1	$\frac{V_o}{2+n+(n+1)D}$	ZCS	200 W	--
[15]	$\frac{2+2n}{1-D}$	1	4	4	1	$\frac{V_o}{2+2n}$	ZCS	300 W	94.43%
[16]	$\frac{2+2n}{1-D}$	2	6	5	2	$\frac{V_o}{2+2n}$	ZCS	--	--
[18]	$\frac{2+2n}{1-D}$	2	6	6	2	$\frac{V_o}{2+2n}$	ZVS/ZCS	400 W	--
[19]	$\frac{2+2n}{1-D}$	2	4	5	3	$\frac{V_o}{2+2n}$	ZCS	--	--
[20]	$\frac{3+n+D}{1-D}$	2	3	3	1	$\frac{V_o}{3+n+D}$	--	600 W	96.2%
[21]	$\frac{2+n+D}{1-D}$	2	4	4	1	$\frac{V_o}{2+n+D}$	--	--	--
[22]	$\frac{1+n+D}{1-D}$	2	4	3	1	$\frac{V_o}{1+n+D}$	ZCS	500 W	--
[24]	$\frac{4}{1-D}$	2	4	4	3	$\frac{V_o}{4}$	ZCS	400 W	93.27%

The simulation waveforms of the input and output voltage are shown in Fig. 15(a). The gating pulse signal of power switches S_1 and S_2 is illustrated in Fig. 15(b). Fig. 15(c) displays the current simulation waveforms obtained from TWCI. To verify the accuracy of theoretical analysis, the voltage and current simulation waveforms of power switches S_1 and S_2 are presented in Fig. 15(d) and (e), respectively. Furthermore, the voltage and current simulation waveforms of diodes $D_1 D_2$, and D_3 are shown in Fig. 15(f) and (g), which have verified the theoretical analysis.

C. Experimental Results Analysis

A 400 W experimental prototype is created to verify the accuracy of ASL-TWCI. And the experimental prototype is shown in Fig. 16.

The experimental results with $V_{in} = 36\,\text{V}$ and $P_o = 400\,\text{W}$ at CCM and the output voltage of $V_o = 400\,\text{V}$ are shown in Fig. 17(a). The leakage inductor currents of TWCI are demonstrated in Fig. 17(b). The voltage and current waveforms of power switches S_1 and S_2 are depicted in Fig. 17(c). The voltage stress of power switches is only about 87 V when the output voltage is 400 V. As illustrated in Fig. 17(d), ZCS turn-ON is attained for power switches. The voltage and current stress waveforms of diode D_1 are depicted in Fig. 17(e). As depicted in Fig. 17(f), the diode D_1 has achieved the ZCS turn-OFF, which eliminates the reverse recovery challenge of diode D_1. The voltage stress of D_1 is only approximately 174 V, which is significantly lower than the output voltage. The voltage and current waveforms of diode D_2 are shown in Fig. 17(g), while Fig. 17(h) demonstrates that D_2 has achieved ZCS turn-OFF, minimizing the reverse recovery challenge of diode D_2. Similarly, Fig. 17(i) depicts the voltage and current waveforms of diode D_3, and Fig. 17(j) shows that D_3 has also achieved ZCS turn-OFF. The voltage stress across D_2 and D_3 is approximately 260 V, which is lower than the output voltage ($V_o = 400\,\text{V}$). Fig. 17(k) illustrates the voltage and current waveforms of output during a rapid change in load,

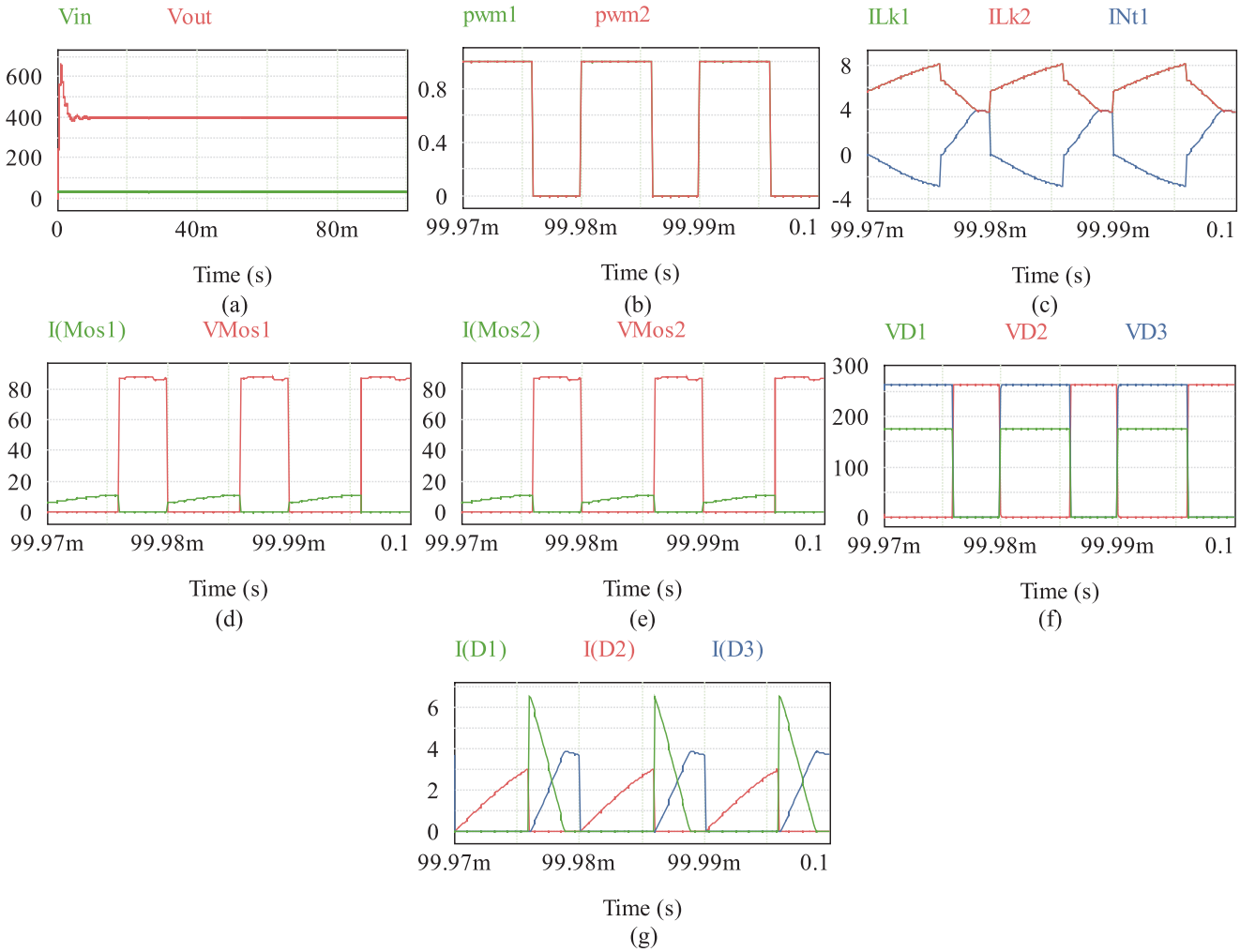

Fig. 15. Simulation waveforms of ASL-TWCI. (a) Input and output voltage. (b) Gating pulse signal. (c) Current of TWCI. (d) Voltage and current stress of power switch S_1. (e) Voltage and current stress of power switch S_2. (f) Voltage of diodes D_1, D_2, and D_3. (g) Current of diodes D_1, D_2, and D_3.

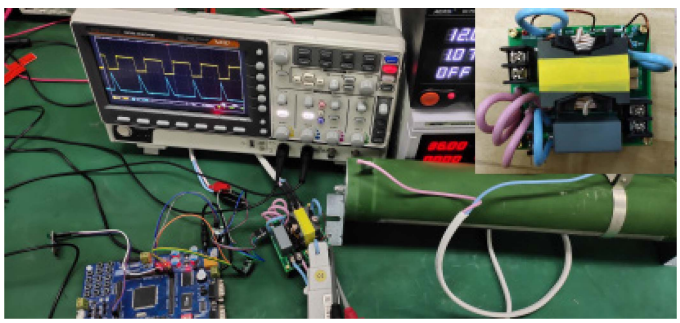

Fig. 16. Photograph of the experimental prototype.

where the output power instantaneously increased from 200 to 400 W when the load is changed.

According to the loss analysis and experimental results of the experimental prototype, the efficiency curve of the proposed ASL-TWCI can be derived, as shown in Fig. 18. The efficiency is highest at rated power of 420 W, with the theoretical efficiency of 97.94% and the measured efficiency of 97.49%. The theoretical efficiency is 97.91% at rated power of 400 W, and the measured efficiency is 97.47%. And the loss of the control system is considered in the other losses.

According to the components selection in Table I, the loss distribution of ALS-TWCI at 400 W is shown in Fig. 19. According to Fig. 19, the main losses of ASL-TWCI are the diodes, magnetic component, and power switches. By selecting components with smaller parasitic parameters, the losses can be further reduced. The losses in the magnetic component can be reduced by using magnetic integration or increasing the cross-sectional area of the wires.

VII. Conclusion

A full soft-switching high step-up dc/dc converter with active switched inductor and three-winding coupled inductor is proposed, which achieves the high voltage conversion ratio without an extremely duty cycle. The ZCS turn-ON performance of power switches is achieved with the assistance of leakage inductor derived from the TWCI. Meanwhile, the ZCS turn-OFF performance of diodes in the modified capacitor clamped cell is achieved by utilizing the leakage inductor from TWCI, which significantly reduces the reverse recovery losses. And the

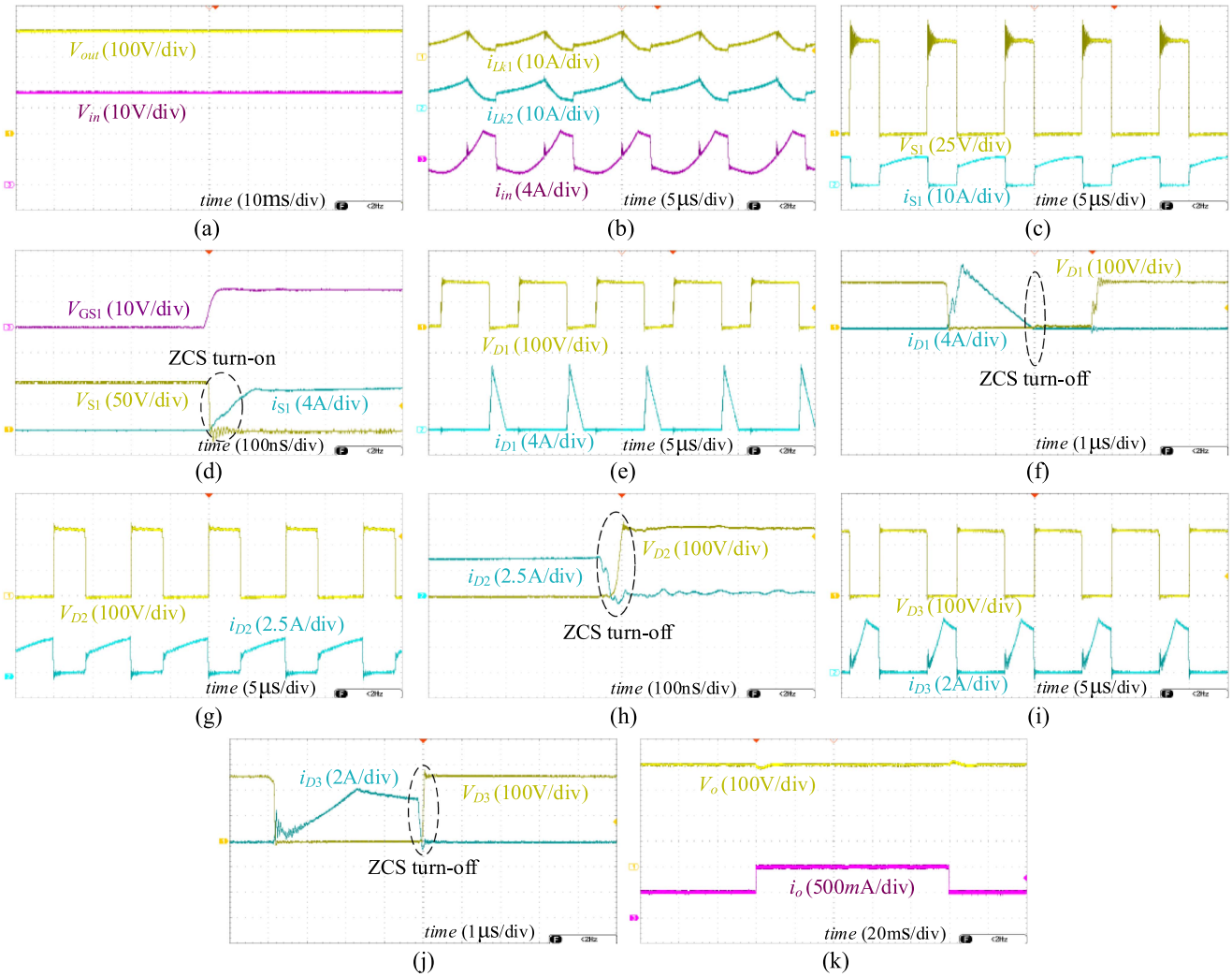

Fig. 17. Experimental waveforms of ASL-TWCI. (a) Input and output voltage. (b) Current of TWCI. (c) Voltage and current stress of power switches. (d) ZCS turn-ON of power switches. (e) Voltage and current stress of diode D_1. (f) ZCS turn-OFF of the diode D_1. (g) Voltage and current stress of diode D_2. (h) ZCS turn-OFF of diode D_2. (i) Voltage and current stress of D_3. (j) ZCS turn-OFF of diode D_3. (k) Dynamic response of the change in load (200–400 W).

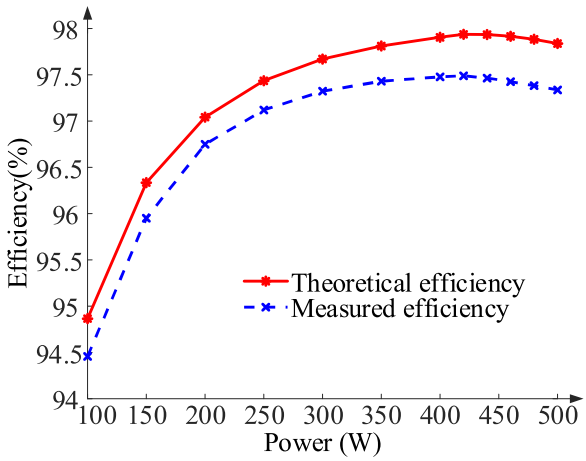

Fig. 18. Theoretical and measured efficiency of ASL-TWCI.

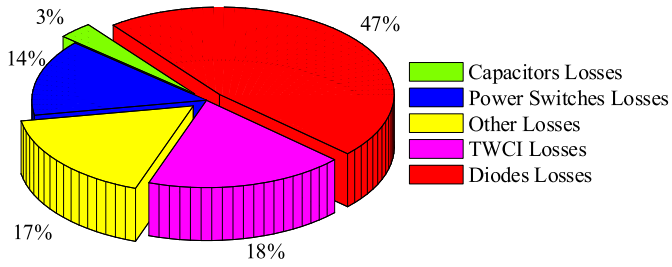

Fig. 19. Loss distribution map when power is 400 W.

ASL-TWCI employs two capacitors in series for the output, with a lower voltage stress compared with the output voltage. Therefore, the capacitors with lower voltage rating and ESR can be chosen, reducing the overall cost and size of ASL-TWCI. Furthermore, the ASL-TWCI achieves other advantages, such as low current and voltage stresses on semiconductors, a simple topological structure and control scheme, and enhanced design flexibility. The operating principles of ASL-TWCI have been analyzed in detail, and its performance has been thoroughly compared with other similar converters. Finally, a 400 W prototype with the input voltage of 36 V and output voltage of 400 V is built, and the experimental results have confirmed the accuracy of theoretical analysis.

REFERENCES

[1] S. A. Ansari and J. S. Moghani, "A novel high voltage gain noncoupled inductor SEPIC converter," *IEEE Trans. Ind. Electron.*, vol. 66, no. 9, pp. 7099–7108, Sep. 2019.

[2] D. Rong, X. Sun, and N. Wang, "A high step-up interleaved boost-Cuk converter with integrated magnetic coupled inductors," *IET Renewable Power Gener.*, vol. 16, no. 3, pp. 607–621, Feb. 2022.

[3] H. Li, L. Cheng, X. Sun, and C. Li, "High step-up combined boost-cuk converter with switched-inductor," *IET Power Electron.*, vol. 15, no. 15, pp. 1664–1674, Nov. 2022.

[4] T. Liu, M. Lin, and J. Ai, "High step-up interleaved DC-DC converter with asymmetric voltage multiplier cell and coupled inductor," *IEEE J. Emerg. Sel. Topics Power Electron.*, vol. 8, no. 4, pp. 4209–4222, Dec. 2020.

[5] L. Schmitz, D. C. Martins, and R. F. Coelho, "Generalized high step-up DC-DC boost-based converter with gain cell," *IEEE Trans. Circuits Syst. I, Reg. Papers*, vol. 64, no. 2, pp. 480–493, Feb. 2017.

[6] M. A. Salvador, T. B. Lazzarin, and R. F. Coelho, "High step-up DC-DC converter with active switched-inductor and passive switched-capacitor networks," *IEEE Trans. Ind. Electron.*, vol. 65, no. 7, pp. 5644–5654, Jul. 2018.

[7] Y. Tang, D. Fu, T. Wang, and Z. Xu, "Hybrid switched-inductor converters for high step-up conversion," *IEEE Trans. Ind. Electron.*, vol. 62, no. 3, pp. 1480–1490, Mar. 2015.

[8] H.-C. Liu and F. Li, "Novel high step-up DC-DC converter with an active coupled-inductor network for a sustainable energy system," *IEEE Trans. Power Electron.*, vol. 30, no. 12, pp. 6476–6482, Dec. 2015.

[9] H. Liu and F. Li, "A novel high step-up converter with a quasi-active switched-inductor structure for renewable energy systems," *IEEE Trans. Power Electron.*, vol. 31, no. 7, pp. 5030–5039, Jul. 2016.

[10] M. A. Salvador, J. M. de Andrade, T. B. Lazzarin, and R. F. Coelho, "Non-isolated high-step-up DC–DC converter derived from switched-inductors and switched-capacitors," *IEEE Trans. Ind. Electron.*, vol. 67, no. 10, pp. 8506–8516, Oct. 2020.

[11] H. Liu, F. Li, and J. Ai, "A novel high step-up dual switches converter with coupled inductor and voltage multiplier cell for a renewable energy system," *IEEE Trans. Power Electron.*, vol. 31, no. 7, pp. 4974–4983, Jul. 2016.

[12] X. Hu, J. Wang, L. Li, and Y. Li, "A three-winding coupled-inductor DC-DC converter topology with high voltage gain and reduced switch stress," *IEEE Trans. Power Electron.*, vol. 33, no. 2, pp. 1453–1462, Feb. 2018.

[13] M. E. Azizkandi, F. Sedaghati, H. Shayeghi, and F. Blaabjerg, "A high voltage gain DC-DC converter based on three winding coupled inductor and voltage multiplier cell," *IEEE Trans. Power Electron.*, vol. 35, no. 5, pp. 4558–4567, May 2020.

[14] S. -K. Changchien, T.-J. Liang, J.-F. Chen, and L.-S. Yang, "Novel high step-up DC-DC converter for fuel cell energy conversion system," *IEEE Trans. Ind. Electron.*, vol. 57, no. 6, pp. 2007–2017, Jun. 2010.

[15] W. Liang, X. Hu, H. Chen, G. Wu, M. Zhang, and G. Tan, "high voltage-gain DC-DC converter with three-winding coupled inductor," *Chin. J. Elect. Eng.*, vol. 5, no. 1, pp. 10–23, Mar. 2019.

[16] W. Li, Y. Zhao, J. Wu, and X. He, "Interleaved high step-up converter with winding-cross-coupled inductors and voltage multiplier cells," *IEEE Trans. Power Electron.*, vol. 27, no. 1, pp. 133–143, Jan. 2012.

[17] S. V. Araujo, R. P. Torrico-Bascope, and G. V. Torrico-Bascope, "Highly efficient high step-up converter for fuel-cell power processing based on three-state commutation cell," *IEEE Trans. Ind. Electron.*, vol. 57, no. 6, pp. 1987–1997, Jun. 2010.

[18] X. Hu, W. Liang, X. Liu, and Z. Yu, "A hybrid interleaved DC-DC converter with a wide step-up regulation range and ultralow voltage stress," *IEEE Trans. Ind. Electron.*, vol. 67, no. 7, pp. 5479–5489, Jul. 2020.

[19] Wuhua Li, W. Li, X. Xiang, Y. Hu, and X. He, "High step-up interleaved converter with built-in transformer voltage multiplier cells for sustainable energy applications," *IEEE Trans. Power Electron.*, vol. 29, no. 6, pp. 2829–2836, Jun. 2014.

[20] T.-J. Liang, P. Luo, and K.-H. Chen, "A high step-up DC-DC converter with three-winding coupled inductor for sustainable energy systems," *IEEE Trans. Ind. Electron.*, vol. 69, no. 10, pp. 10249–10258, Oct. 2022.

[21] K. Takahashi, A. Matsuda, Y. Nakagawa, and H. Koizumi, "A high step-up dual switches dc-dc converter with three-winding coupled inductor and charge pump," in *Proc. IEEE Energy Convers. Congr. Expo.*, Portland, OR, USA, 2018, pp. 1253–1258.

[22] Y. Tang, D. Fu, J. Kan, and T. Wang, "Dual switches DC/DC converter with three-winding-coupled inductor and charge pump," *IEEE Trans. Power Electron.*, vol. 31, no. 1, pp. 461–469, Jan. 2016.

[23] H. Li, W. Wang, Y. Zeng, Y. Zhao, and Y. Jiang, "A 3L capacitor clamping dc-dc converter with low current ripple and high voltage gain," in *Proc. IEEE Energy Convers. Congr. Expo.*, Baltimore, MD, USA, 2019, pp. 4366–4371.

[24] H. Li, H. Du, Y. Zeng, Z. Qiu, X. Jiang, and Z. Chen, "A modified interleaved capacitor clamped DC–DC converter with non-resonant soft switching," *IEEE Trans. Power Electron.*, vol. 37, no. 10, pp. 12221–12236, Oct. 2022.

[25] Y. Zeng, H. Li, W. Wang, B. Zhang, and T. Q. Zheng, "Cost-effective clamping capacitor boost converter with high voltage gain," *IET Power Electron.*, vol. 13, no. 9, pp. 1775–1786, Jul. 2020, doi: 10.1049/iet-pel.2019.1291.

[26] Y. Zeng, H. Li, W. Wang, B. Zhang, and T. Q. Zheng, "High-efficient high voltage-gain capacitor clamped DC–DC converters and their construction method," *IEEE Trans. Ind. Electron.*, vol. 68, no. 5, pp. 3992–4003, May 2021.

Chao Li (Graduate Student Member, IEEE) was born in Anhui Province, China, in 1999. He received the B.S. degree in smart grid information engineering in 2021 from Liaoning Technical University, Huludao, China, where he is currently working toward the M.S. degree in power electronics and power transmission.

His current research interests include power electronics' applications and magnetic integration in power electronics.

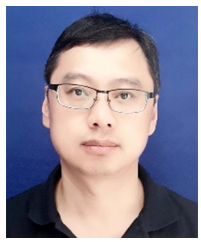

Hongzhu Li (Member, IEEE) was born in Heilongjiang Province, China, in 1974. He received the B.S., M.S., and Ph.D. degrees in electrical and control engineering from Liaoning Technical University, Huludao, China, in 1998, 2005, and 2020, respectively.

He is currently working as a Professor with the Faculty of Electrical and Control Engineering, Liaoning Technical University, Huludao, China. His current research interests include power electronic converter and its magnetic device integration technology and switching converter electrical intrinsic safety technology.

Ning Wang was born in Shanxi Province, China, in 1994. He received the M.S. degree in electrical engineering from Liaoning Technical University, Huludao, China, in 2022. He is currently working toward the Ph.D. degree in power electrical engineering with the China University of Mining and Technology, Beijing, China.

His current research interests include power converters and high-frequency transformer.

Xuanjin Sun (Student Member, IEEE) was born in Tianjin, China, in 1993. He received the M.S. degree in electronic engineering in 2020 from Liaoning Technical University, Huludao, China, where he is currently working toward the Ph.D. degree in power electrical engineering.

His current research interests include magnetic integration in power electronics and high step-up converters.

Lihong Cheng was born in Liaoning Province, China, in 1997. He received the B.S. degree in smart grid information engineering in 2020 from Liaoning Technical University, Huludao, China, where he is currently working toward the M.S. degree in power electronics and power transmission.

His current research interests include magnetic components in high step-up converters.